

Nonequilibrium Charge-Density-Wave Order Beyond the Thermal Limit

J. Maklar¹, Y. W. Windsor¹, C. W. Nicholson^{1,*}, M. Puppini^{1,†}, P. Walmsley^{2,3}, V. Esposito^{3,4}, M. Porer⁴, J. Rittmann⁴, D. Leuenberger⁵, M. Kubli⁶, M. Savoini⁶, E. Abreu⁶, S. L. Johnson⁶, P. Beaud⁴, G. Ingold⁴, U. Staub⁴, I. R. Fisher^{2,3}, R. Ernstorfer¹, M. Wolf¹, and L. Rettig¹

¹*Fritz-Haber-Institut der Max-Planck-Gesellschaft, Faradayweg 4-6, D-14195 Berlin, Germany*

²*Geballe Laboratory for Advanced Materials and Department of Applied Physics, Stanford University, CA 94305, USA*

³*Stanford Institute for Materials and Energy Sciences, SLAC National Accelerator Laboratory, 2575 Sand Hill Road, Menlo Park, CA 94025, USA*

⁴*Swiss Light Source, Paul Scherrer Institut, CH-5232 Villigen PSI, Switzerland*

⁵*Department of Physics, University of Zürich, CH-8057 Zürich, Switzerland*

⁶*Institute for Quantum Electronics, Physics Department, ETH Zürich, CH-8093 Zürich, Switzerland*

January 20, 2022

The interaction of many-body systems with intense light pulses may lead to novel emergent phenomena far from equilibrium. Recent discoveries, such as the optical enhancement of the critical temperature in certain superconductors and the photo-stabilization of hidden phases, have turned this field into an important research frontier. Here, we demonstrate nonthermal charge-density-wave (CDW) order at electronic temperatures far greater than the thermodynamic transition temperature. Using time- and angle-resolved photoemission spectroscopy and time-resolved X-ray diffraction, we investigate the electronic and structural order parameters of an ultrafast photoinduced CDW-to-metal transition. Tracking the dynamical CDW recovery as a function of electronic temperature reveals a behaviour markedly different from equilibrium, which we attribute to the suppression of lattice fluctuations in the transient nonthermal phonon distribution. A complete description of the system's coherent and incoherent order-parameter dynamics is given by a time-dependent Ginzburg-Landau framework, providing access to the transient potential energy surfaces.

Introduction

Complex solids exhibit a multitude of competing and intertwined broken symmetry states originating from a delicate interplay of different degrees of freedom and dimensionality. Among these states, charge-density-waves (CDWs) are a ubiquitous phase characterised by a cooperative periodic modulation of the charge density and of the crystal lattice, mediated by electron-phonon coupling^{1–3}. While lattice and charges are intrinsically coupled in equilibrium, ultrafast optical excitation allows to selectively perturb each of these subsystems and to probe the melting of order and its recovery as a real-time process. This

Current address:

*Department of Physics and Fribourg Center for Nanomaterials, University of Fribourg, Chemin du Musée 3, CH-1700 Fribourg, Switzerland

†Laboratory of Ultrafast Spectroscopy, ISIC, Ecole Polytechnique Fédérale de Lausanne (EPFL), CH-1015 Lausanne, Switzerland

approach grants access to the relevant interactions of CDW formation^{4–15}, to out-of-equilibrium and metastable states^{16–19} and elucidates competing orders^{20–22}.

In close analogy to superconductivity, the formation of a CDW broken symmetry ground state can be described by an effective mean field that serves as an order parameter, which is governed in equilibrium by a static free energy surface. While mean field theory captures the phase transition on a qualitative level, thermal lattice fluctuations reduce the critical temperature T_c of long-range 3D order significantly below the predicted mean field value T_{MF} ^{1,2}. It is of strong interest how our understanding of phase transitions in the adiabatic limit can be adapted to a non-equilibrium, dynamical setting induced by an impulsive excitation^{11,23–27}. It remains an open question whether the thermal transition temperature is still a relevant quantity in the description of such an out-of-equilibrium state, and which parameters permit transient control of T_c ^{20,28–32}.

Symmetry-broken phases also allow for collective excitations of the order parameter, as observed in a variety of systems, including CDW compounds, superconductors and atoms in optical lattices^{33–35}. Two types of modes emerge in the symmetry-broken ground state, related to a variation of the amplitude and the phase of the complex order parameter, i.e., the Higgs amplitude mode (AM) and the Nambu-Goldstone phase mode. In CDW compounds, upon impulsive excitation, the AM manifests as coherent oscillations of the electronic and structural order-parameter amplitudes^{4,6,36}. However, recent studies investigating the structural dynamics of various CDW compounds upon strong perturbation hint towards collective modes at increased frequencies far beyond the intrinsic AM^{11,26,37}.

To address these issues, we investigate the electronic and structural order of optically excited bulk TbTe₃, a prototypical CDW compound of the rare-earth tritelluride family^{38,39}. Using time- and angle-resolved photoemission spectroscopy (trARPES) in combination with time-resolved X-ray diffraction (trXRD), schematically depicted in Fig. 1a, we extract the amplitude of the electronic and structural order parameters and the electronic temperature as functions of pump-probe delay t . This reveals CDW formation at electronic temperatures substantially above the thermal critical temperature. We attribute this transient stabilization to a reduced contribution of lattice fluctuations in the out-of-equilibrium state due to a nonthermal phonon population. Furthermore, with increasing excitation density, the coherent order parameter dynamics indicate a transition from the AM regime to a high-frequency regime, driven by a modification of the underlying potential energy surface. We model the order-parameter dynamics in a time-dependent Ginzburg-Landau framework, which further supports the scenario of a nonthermal stabilization of the CDW order.

Results

Electronic and structural CDW signatures

First, using ARPES, we analyse the Fermi surface (FS) of TbTe₃ at $T = 100$ K, well below $T_c = 336$ K, the transition temperature of the unidirectional CDW phase⁴⁰. The electronic properties near E_F are governed by the Te sheets (Fig. 1a), which give rise to the diamond-shaped bands shown in Fig. 1b. Strongly wave-vector dependent electron-phonon coupling⁴¹, in conjunction with a moderately well-nested Fermi surface⁴², lead to a unidirectional CDW in which some portions of the Fermi surface are gapped while others remain metallic³⁹. To study the effect of the CDW on the lattice, we investigate the intensity of superlattice (SL) Bragg peaks using trXRD. These SL peaks arise from the periodic lattice distortion associated with the CDW, and are displaced by the CDW wave vector $\pm \mathbf{q}_{CDW}$ from the main peak positions^{40,43}. As Fig. 1c shows, photoexcitation strongly suppresses the SL peak corresponding to a rearrangement of the atomic mean positions towards the trivial metallic phase, while the main lattice peak reflecting the average crystal structure shows only minor changes.

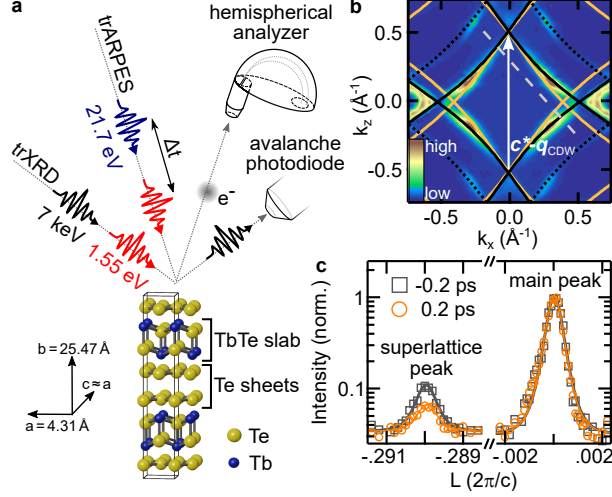


Fig. 1: Experimental scheme. (a) Schematic of the trARPES and grazing-incidence trXRD experiments. TbTe₃ is a quasi-2D compound consisting of a stack of Te sheets and TbTe slabs. (b) Symmetrized FS of TbTe₃ ($T = 100 \text{ K}$, $t = 0 \text{ fs}$). Below T_c , the spectral weight within the nested FS regions connected by the CDW wave vector $c^* - q_{\text{CDW}}$ vanishes³⁹. The black solid and dotted lines correspond to Te 5p_x/5p_z bands from tight-binding calculations. FS nesting also leads to the formation of shadow bands (orange lines). The grey dashed line indicates the momentum-direction analysed in Figs. 2a-c. (c) Representative X-ray Bragg peaks with Voigt fits along the $(3 \ 7 \ L)$ direction before and after optical excitation (absorbed fluence $F = 1.35 \text{ mJ cm}^{-2}$).

Next, we investigate the electron dynamics associated with the CDW upon photoexcitation. We focus on an energy-momentum cut that contains the electronic signatures of the CDW, namely the energy gap at E_F in the nested regions and the backfolded shadow bands⁴⁴, shown in Figs. 2a-b. At temporal pump-probe overlap ($t = 0 \text{ fs}$), the interacting tight-binding model introduced by Brouet et al.³⁹ is in excellent agreement with the observed quasiparticle dispersion: In the nested region (left side of Figs. 2a-b), we observe a pronounced hybridization energy gap at E_F . In the imperfectly nested region (right side), the Te band exhibits metallic behaviour, as the energy gap is located above E_F . Furthermore, we observe faint shadow bands in the vicinity of the energy gaps (boxes 2 and 3 in Fig. 2b). Within 120 fs, the system undergoes a photoinduced CDW-to-metal transition⁶, as apparent from the transient suppression of the energy gap and the shadow bands, see Figs. 2c-e.

CDW order-parameter dynamics

The CDW-to-metal transition can be described by an order parameter ψ , with $|\psi| = 0$ in the metallic and $0 < |\psi| \leq 1$ in the CDW phase. Due to the coupling between charges and lattice, the transition can be characterized by an electronic (ψ_e) or a structural (ψ_s) order parameter. We utilize trARPES to access the amplitude of the electronic order parameter $|\psi_e|$. Most directly, $|\psi_e|$ can be extracted by tracking the energy gap 2Δ at E_F ^{13,45}. However, this method faces practical limitations due to the vanishing occupation of bands above E_F after a few 100 fs and due to the limited experimental energy resolution. Therefore, we choose two alternative metrics to quantify the CDW order: We introduce the inverted in-gap intensity $\tilde{I}_{\text{in-gap}} = 1 - I_{\text{in-gap}}$ with normalized in-gap intensity $I_{\text{in-gap}}$, extracted from box 1 in Fig. 2b. We find that this metric – for the chosen region of interest and our experimental resolution – follows a BCS-like temperature dependence in equilibrium, as confirmed by static measurements (black markers in Fig. 3b), and thus is considered equivalent to $|\psi_e|$. Further, as the inverted in-gap intensity is derived from a region where the gap is centered around E_F , it is unaffected by thermal changes to the distribution function. As a second metric, we extract the shadow band intensity $I_{\text{SB}} \propto |\psi_e|$ ^{30,44} from box 2 in Fig. 2b.

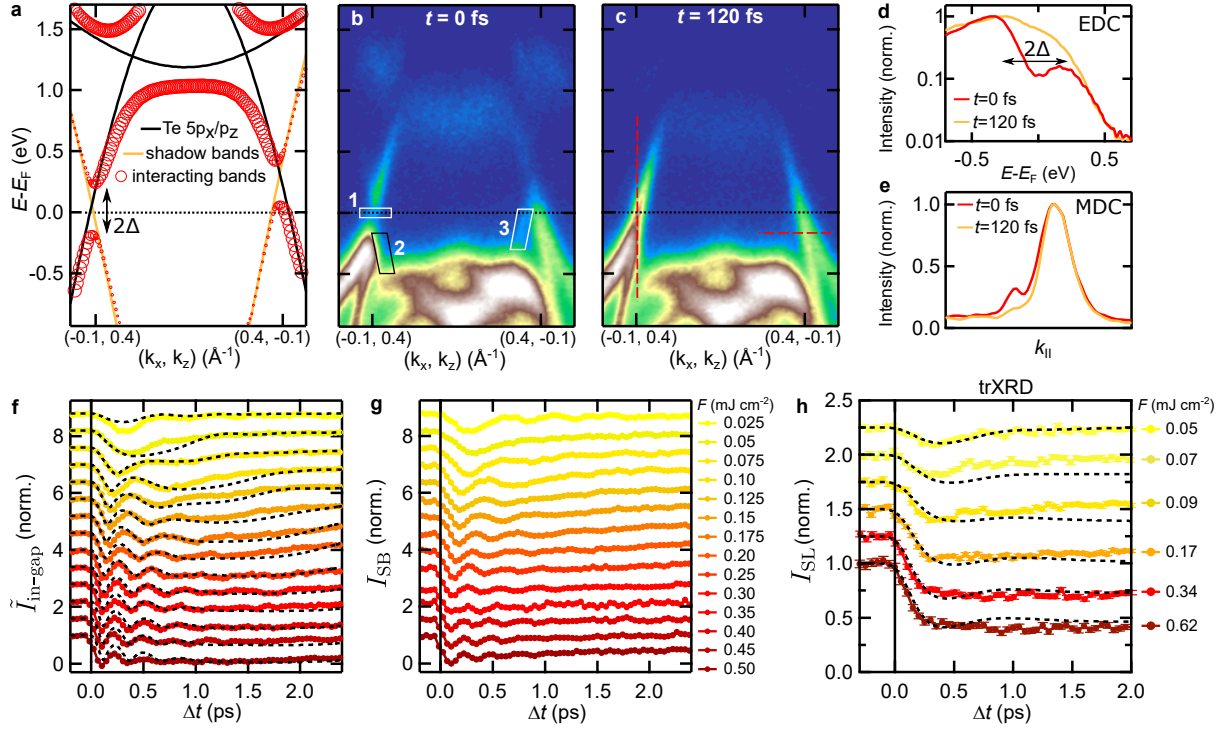


Fig. 2: CDW band structure dynamics. (a) Tight-binding bands along the momentum-direction indicated by the dashed grey line in Fig. 1b. The black and orange curves correspond to the non-interacting Te main and shadow bands, respectively. The red circles mark the hybridized bands with interaction potential Δ . The circle size illustrates the spectral weight. (b-c) trARPES measurements ($F = 0.45 \text{ mJ cm}^{-2}$) along the momentum direction shown in a. At $t = 0$ fs, the energy gap at E_F (box 1) and shadow bands (boxes 2, 3) indicate the CDW order. After 120 fs, the CDW vanishes, and the energy gap and shadow band intensity are strongly suppressed. (d-e) Energy and momentum distribution curves along the dashed vertical and horizontal lines in c, respectively. (f) Inverted in-gap intensity $\tilde{I}_{\text{in-gap}} = 1 - I_{\text{in-gap}}$ with in-gap intensity $I_{\text{in-gap}}$ (box 1 in b, normalized by the respective pre-excitation values) as function of pump-probe delay for various fluences (displaced vertically). Normalized time-dependent Ginzburg-Landau simulations are shown in black. For details of the model, see main text and Supplementary Note B. (g) Normalized shadow band intensity extracted from box 2. The shadow band intensity obtained from box 3 is shown in Supplementary Fig. 1. (h) Time evolution of the (2 10 1+ q_{CDW}) SL peak intensity for various fluences (displaced vertically) with layered Ginzburg-Landau simulations, see Supplementary Note D. The curves are normalized by their respective pre-excitation values. The error bars correspond to one standard deviation from photon counting statistics.

Using these equivalent metrics, we investigate the photoinduced CDW suppression and recovery over a wide range of fluences, as shown in Figs. 2f-g. For a low absorbed fluence of 0.025 mJ cm^{-2} below the CDW melting threshold, we observe a weak modulation of the CDW gap and SB intensity corresponding to the AM of the CDW at $\omega_{\text{AM}}/2\pi = 2.2 \text{ THz}$ (see Supplementary Fig. 2). At the CDW melting threshold $\approx 0.05 \text{ mJ cm}^{-2}$, the AM softens and becomes overdamped, while the CDW melting time t_{melt} slows down, and the energy gap and SB intensity vanish almost completely. Upon crossing the melting threshold, we observe a fast initial quench of the CDW within $t_{\text{melt}} \approx 100 \text{ fs}$ (see Supplementary Fig. 8), followed by few damped coherent oscillations that exhibit a pronounced frequency reduction with pump-probe delay (down-chirp). Interestingly, the initial frequency of the collective excitation increases with fluence, doubling at the highest accessible fluences. Concurrently, the time required to restore the ground state after perturbation steadily increases with fluence, leading to a persistent suppression of the CDW for a few ps at the highest excitation densities we used.

To gain a complementary view of the photoinduced phase transition, we use trXRD to extract the structural order parameter from the normalized SL peak intensity upon optical excitation^{11,23,37}, which, in first approximation, is given by $I_{\text{SL}}(t) \propto |\psi_s(t)|^2$. As Fig. 2h shows, the SL response qualitatively

resembles the dynamical quench and recovery of the extracted electronic order parameter. In the low-fluence regime, a weak initial suppression is followed by a quick recovery of the SL structure, on top of which a faint modulation can be identified (see Supplementary Fig. 3). In the high-fluence regime, the SL peak intensity is strongly quenched, and, with increasing fluence, the time required to recover diverges. In contrast to the electronic response, we do not observe clear coherent oscillations of the SL peak intensity upon strong excitation. This originates most likely from the lower temporal resolution of the trXRD setup and the contribution of sub-surface crystal layers with varying, lower excitation densities (see Supplementary Note D). Recent trXRD experiments with improved temporal resolution have revealed fluence-dependent collective excitations of the SL peak intensity in a closely related tritelluride³⁷ – in agreement with our observations for ψ_e . Furthermore, while the SL intensity I_{SL} drops linearly with excitation density shortly after excitation, this behaviour plateaus after crossing a fluence of $\approx 0.1 \text{ mJ cm}^{-2}$. This results in a residual SL intensity of 35% even after strong excitation of up to 1.35 mJ cm^{-2} . We assign this persisting SL background to a contribution of unexcited sample volumes due to surface steps caused by crystal cleaving¹¹. Nonetheless, the trXRD data clearly shows that not only the electronic, but also the lattice superstructure is melted upon strong photoexcitation. The qualitative agreement of the electronic and structural response demonstrates a strong coupling between electronic and lattice degrees of freedom on ultrafast timescales, and suggests an equivalent treatment of $|\psi_s|$ and $|\psi_e|$ within the experimental time resolution.

Diffraction also probes the long-range coherence of the SL phase. While phase coherence plays a secondary role in the low-fluence regime, it becomes increasingly important during the CDW recovery after strong perturbation due to the creation of topological defects. These dislocation-type defects broaden the SL peaks, locally decrease the amplitude of the periodic lattice modulation, and can persist long after the CDW amplitude has recovered^{46–48}. Therefore, rather than trXRD, we employ trARPES to access the amplitude of the order parameter throughout the full recovery to equilibrium. As shown in Fig. 3a, in the high-fluence regime, the majority of the CDW order is restored after $\approx 5 \text{ ps}$, followed by a complete recovery on a 100 ps timescale.

Transient electronic temperature

Time-resolved ARPES allows to extract the transient electronic temperatures from Fermi-Dirac fits to the energy distribution of metallic regions of the FS (see Supplementary Note C), and thereby to compare the non-equilibrium CDW melting and recovery to the mean field behaviour upon thermal heating. Remarkably, in the dynamic case, the electronic order parameter does not follow the mean field dependence governed by T_c . In the low-fluence regime below the CDW melting threshold, electronic temperatures reach up to 500 K , far above $T_c = 336 \text{ K}$ (see Supplementary Fig. 7a). Yet, photoexcitation causes only a minor initial suppression of the energy gap and of the periodic lattice distortion, and initiates a collective AM oscillation – a hallmark of the CDW state.

In the high-fluence regime, the CDW is fully suppressed ($\tilde{I}_{\text{in-gap}} = I_{\text{SB}} = 0$) as initial electronic temperatures exceed 2000 K . However, recovery of the CDW order already sets in when the electronic system is still at elevated temperatures $T_e \gg T_c$. To illustrate this dynamic behaviour, Fig. 3b presents the inverted in-gap intensity of the melting and the recovery cycle as a function of extracted electronic temperatures. In the out-of-equilibrium setting, CDW order reappears below $T_e \approx 600 \text{ K}$ (yellow shaded area), indicating an increased effective critical temperature T_c^* . At delay times of several ps, corresponding to electronic temperatures of $T_e \leq T_c$, the dynamic behaviour converges to the equilibrium T -dependence. This trend of nonthermal CDW recovery is consistent over a wide range of fluences (see Supplementary Fig. 4).

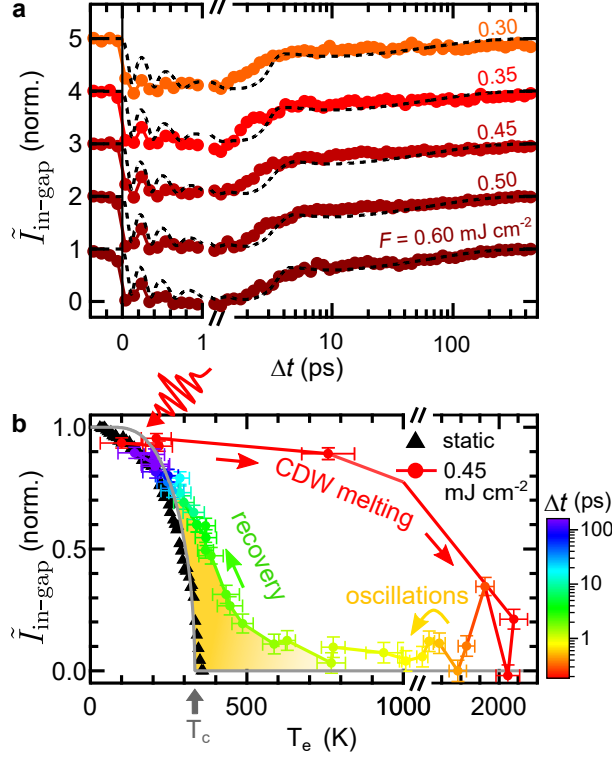


Fig. 3: CDW recovery dynamics. (a) Time evolution of the inverted in-gap intensity in the high-fluence regime (displaced vertically). Normalized time-dependent Ginzburg-Landau simulations are shown in black. (b) Inverted in-gap intensity versus extracted electronic temperatures. One standard deviation of the T_e fit (horizontal error bars) and one standard deviation derived from electron counting statistics (vertical error bars) are given as uncertainty. $\tilde{I}_{\text{in-gap}}$ extracted from a static temperature series (black markers, T -values from heater setpoints, curve normalized to the lowest accessible T -value) is in general agreement with the BCS-type T -dependence of the order parameter (grey curve). The dynamic trace shows the full cycle of laser-heating and CDW melting, coherent oscillations and CDW recovery (delay encoded in the color code). The yellow shaded area marks the region of dynamical CDW formation at electronic temperatures above T_c . The pre-excitation value of the dynamic trace ($T = 100$ K) is normalized to the corresponding value of the static T -dependence.

Time-dependent Ginzburg-Landau theory

Near the transition temperature, the order parameter can be approximated by the Landau theory of second-order phase transitions². Thus, to simulate the dynamics of the order parameter in TbTe_3 , we make the following ansatz for the effective potential energy surface (in dimensionless units) based on time-dependent Ginzburg-Landau (tdGL) theory^{11,27,37,49,50}:

$$V(\psi, t) = -\frac{1}{2}(1 - \eta(t))\psi^2 + \frac{1}{4}\psi^4. \quad (1)$$

Upon perturbation, the dynamics of the order parameter are determined by the equation of motion derived from Eq. 1 (see Supplementary Note B). The transient modification of the potential, resulting from the laser excitation and subsequent relaxation, is modelled by the ratio of the electronic temperature and the critical temperature $\eta(t) = T_e/T_c$. Motivated by the increased transient ordering temperature discussed above, we replace the static T_c by a phenomenological time-dependent critical temperature

$$T_c^*(t) = T_c \left(1 + H(t) \cdot s \cdot \exp(-t/\tau_{\text{ph-ph}}) \right), \quad (2)$$

with Heavyside step function H . It captures the enhanced critical temperature in the nonthermal regime, given by the temperature scaling s , and converges to T_c at late times. This leaves us with only two global

fit parameters for the simulations: damping γ and scaling s in the nonthermal regime (see Supplementary Note B for details of the model). For the timescale connecting both regimes, we find a good description of the data by choosing the lattice thermalization time $\tau_{\text{ph-ph}} = 2.2$ ps reported for the closely related compound LaTe_3 ²⁷. Energy redistribution processes within the electron and lattice systems are often modelled by a three temperature model (3TM)^{51,52}, as presented in Fig. 4c. Here, $\tau_{\text{ph-ph}}$ corresponds to the timescale of energy transfer between strongly coupled optical phonon modes ($T_{\text{hot-ph}}$) with the remaining cold lattice modes (T_l). The choice of the parameter $\tau_{\text{ph-ph}}$ is further motivated in the following discussion. In this description, CDW order emerges when the electronic temperature T_e falls below the introduced dynamic effective T_c^* (black dashed curve in Fig. 4c). During the thermalization process, the estimated lattice temperatures T_l stay below the thermal critical temperature for all applied fluences.

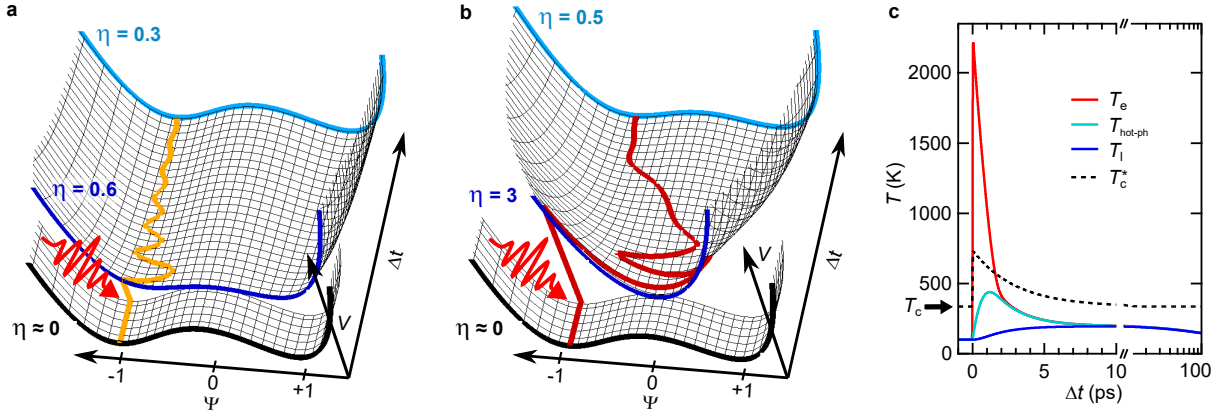


Fig. 4: Simulated order-parameter dynamics and 3TM. Transient potential energy surface and order-parameter pathway upon (a) weak and (b) strong optical excitation. The potential shapes before excitation (black curve), at 0 ps (dark blue) and 3.5 ps (light blue) are highlighted. (a) In the AM regime, the double-well potential is weakly modified, while in (b) the overshoot regime, the CDW melting threshold is reached, resulting in a single-well shaped potential, followed by a relaxation to the double-well ground state. (c) 3TM of electronic, hot phonon and lattice temperatures T_e , $T_{\text{hot-ph}}$ and T_l in the regime of strong perturbation ($F=0.35$ mJ cm⁻²). In the 3TM, the optical excitation of the electronic system is followed by an energy transfer to certain strongly-coupled optical phonons, widely observed in materials with selective electron-phonon coupling^{27,51–55}. Subsequently, this hot phonon subset equilibrates with the remaining lattice phonon bath on a ps timescale ($\tau_{\text{ph-ph}}$). To account for the recovery of the base temperature via heat diffusion on a 100 ps timescale, the lattice is coupled to an external heat sink. The black dashed line indicates the rescaled critical temperature T_c^* . In the 3TM simulations, material properties of the related compound LaTe_3 ²⁷ were used.

Given the complexity of the system, this model with its minimal amount of free parameters is in remarkable agreement with the electronic order parameter extracted directly from the trARPES data throughout the CDW melting and full recovery over a large fluence range, as shown in Figs. 2f and 3a. It captures (i) the AM in the low-fluence regime, (ii) the CDW melting time after arrival of the pump, (iii) the coherent oscillations and the down-chirp in the high-fluence regime, and (iv) the full CDW recovery to equilibrium. The fit yields a nonthermal critical temperature of $T_c^*(t = 0 \text{ fs}) \approx 745$ K, i.e., more than double of the equilibrium T_c . Remarkably, this value is similar to the electronic temperature where the onset of CDW recovery is observed in Fig. 3b. To illustrate the necessity of a transiently enhanced T_c^* to describe the data, we perform tdGL simulations keeping the critical temperature fixed at the equilibrium value, which, however, leads to a severe deviation from the experimental oscillations and CDW recovery, see Supplementary Fig. 5. Next, we illustrate the characteristic regimes of the tdGL simulations based on the extracted transient potential energy surfaces $V(\psi, t)$ in Fig. 4.

AM regime: Before excitation, the system is in the CDW ground state ($\eta \approx 0$), corresponding to an underlying double-well potential with minima at $|\psi| \approx 1$. Upon weak excitation (Fig. 4a), the potential surface is barely altered and maintains its double-well shape. This launches a damped oscillation of the

order parameter around the marginally shifted potential minimum at frequency ω_{AM} , i.e., the AM.

Overshoot regime: Upon strong excitation (Fig. 4b), the underlying potential transforms to a single-well shape, corresponding to the metallic phase. The order parameter overshoots to the opposite side of the potential, and oscillates around the new potential minimum at $|\psi| = 0$ at frequency $\omega \gg \omega_{\text{AM}}$. Relaxation of the system leads to a transient flattening of the potential, resulting in the observed frequency down-chirp. At $\eta < 1$, the CDW order finally recovers, and the order parameter relaxes into one of the minima of the emerging double-well potential.

A minor deviation of the fit from the data occurs at the dynamical slowing-down of the CDW melting in the vicinity of the melting threshold, as observed in the curve at fluence 0.05 mJ cm^{-2} in Fig. 2f. For an initial perturbation in the range $\eta_{\text{init}} \approx 0.5 \dots 1$, the system gains just enough energy to reach the local maximum of the double-well potential at $|\psi| = 0$. Close to this metastable point, the potential is rather flat, leading to a critical slowing-down of the order-parameter dynamics⁵⁶, discussed in detail in Supplementary Note E. A similar critical behaviour is expected during the recovery of the CDW order. In the overshoot regime, after dampening of the initial oscillations, the order parameter can get trapped at the metastable local maximum despite an incipient recovery of the double-well ground state. However, in real systems, several microscopic processes, such as local modification of T_c by crystal defects^{57,58}, CDW nucleation and creation of topological defects⁴⁷ and coupling of the collective excitation to other phonons³⁶, will screen against a pronounced critical slowing-down. However, such effects go beyond our current model.

To reproduce the main observations of the extracted structural order parameter, we extend this model to a layered description (see Supplementary Note D), as shown in Fig. 2h. However, the absence of clear coherent modulations in the time evolution of the SL peak intensity and the additional contribution of the SL phase coherence prohibit a reliable fit of $I_{\text{SL}}(t)$. Nonetheless, we conclude that this model captures all key features of the structural and electronic order parameters within a unified framework.

Discussion

We unambiguously demonstrate a transient CDW behaviour distinct from equilibrium, as evidenced by the CDW AM modulations after weak excitation despite electronic temperatures exceeding thermal T_c , and from the CDW recovery at elevated electronic temperatures after strong excitation. The qualitative correspondence of charge and structural features of the CDW excludes a scenario in which only the electronic superstructure is destroyed while the lattice distortion remains intact, which could facilitate such a nonthermal behaviour. So what causes this enhanced transient stability of CDW order far beyond the equilibrium T_c ? In equilibrium, lattice fluctuations induced by thermally populated phonons, accompanied by fluctuations of the charge density, reduce T_c significantly below the mean-field value T_{MF} . Especially in low-dimensional systems, these fluctuation effects become increasingly important, such that long-range order and phase transitions cannot occur at finite temperatures in strictly 1D systems^{1,2}. However, in real materials, coupling between neighbouring chains stabilizes the CDW order, resulting in short-range correlations at high-temperatures and long-range 3D order below $T_c^{2,3}$.

Ultrafast optical perturbation breaks the thermal equilibrium between charges and lattice. Initially, electrons and certain optical phonons are strongly excited, while the overall vibrational population of the lattice – determined by acoustic modes that account for the majority of the lattice heat capacity – is still close to its pre-excitation value corresponding to an effective lattice temperature significantly below T_c . In this out-of-equilibrium regime, the average displacement of the ionic cores around their mean positions (mean-squared displacement) is small, as the nonthermal phonon population is dominated by high-frequency, low-amplitude optical phonons⁵⁹. Thus, initially after excitation, lattice fluctuations

are strongly suppressed and counteract a mean-field long-range ordering only weakly, which facilitates CDW formation even at electronic temperatures far beyond T_c , illustrated in Fig. 5. In this nonthermal regime, T_c is replaced by the effective electronic critical temperature T_c^* , which is renormalized towards the mean field value depending on the transient lattice temperature and concomitant fluctuations. Over the course of several ps, depending on the lattice thermalization time $\tau_{\text{ph-ph}}$, energy is transferred from the strongly coupled optical hot phonons to the remaining phonon modes. This defines the crossover from the nonthermal to the quasi-thermal regime, at which electrons and lattice locally reach thermal equilibrium. As the lattice temperature rises, acoustic (high-amplitude) fluctuations and CDW phase fluctuations increase, which impedes long-range 3D CDW order, and T_c^* consequently converges towards the equilibrium T_c . The increasing occupation of lattice vibrations also increases the lattice entropy, and thus modifies the underlying free energy surface. In this picture, the changing lattice entropy plays the analogous part to the time-dependent critical temperature introduced within our tdGL expansion.

The agreement of the Ginzburg-Landau simulations with the extracted order parameters further underlines this scenario. The initial oscillation frequency of the electronic order parameter, the down-chirp as well as the recovery are reproduced by simulations with an enhanced T_c^* , that converges towards the equilibrium T_c on the lattice thermalization time. In addition, since the initial lattice temperature is close to its equilibrium value also after strong excitation to the overshoot regime, the contribution of thermal fluctuations is expected to be rather independent of fluence. This is in agreement with our model, which captures the experimental data over a wide fluence range with a fluence-independent description of T_c^* . Our simulations yield a transient critical temperature of ≈ 750 K at early times, which is still considerably below the mean field transition temperature $T_{\text{MF}} \approx 1600$ K estimated from the electronic energy gap in the nested regions via the well-known BCS expression². However, because of the imperfect nesting of large segments of the FS, a significant reduction of T_{MF} is expected^{40,60}, and remaining fluctuations at the initial lattice temperature of $T_l \approx 100$ K are further expected to lead to a lower T_c^* .

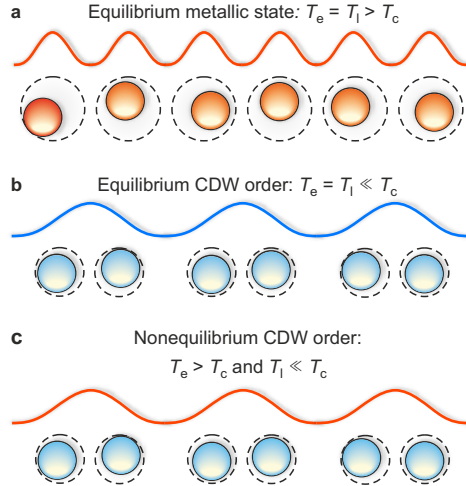


Fig. 5: Illustration of nonthermal CDW order. (a) In equilibrium at elevated temperatures, the system is in a trivial metallic phase. The charge density (wavy line) and the mean positions of the ionic cores (circles) are spaced evenly, as strong thermal lattice fluctuations prevent long-range CDW order. (b) In equilibrium at low temperatures, the system features an ordered charge- and lattice superstructure. (c) Photoexcitation of the CDW ground state ($T_{\text{pre-exc.}} \ll T_c$) generates a hot electron distribution, while the lattice initially remains cold. In this out-of-equilibrium state, thermal lattice fluctuations are weak and barely hinder long-range CDW ordering. Hence, the charge and lattice superstructure is stabilized at electronic temperatures beyond T_c .

The CDW order above T_c may be further stabilized by transiently enhanced FS nesting. A previous

trARPES study has demonstrated an improved nesting condition in rare-earth tritellurides upon optical excitation¹³, caused by a transient modification of the FS. Consequently, the CDW-gapped area at E_F expands and the critical temperature transiently increases. However, the photoinduced enhanced nesting significantly increases with excitation density¹³, which would result in a strongly fluence-dependent nonthermal critical temperature. As we find a good description of the data by T_c^* independent of fluence, we assign a suppression of lattice fluctuations in the out-of-equilibrium state as the dominant effect stabilizing the transient CDW. Several studies suggest similar nonthermal behaviour in other CDW materials. The commensurate CDW phase of 1T-TaS₂ exhibits an exceptionally robust AM after strong perturbation, with initial electronic temperatures exceeding 1300 K⁵. In elemental Chromium, trXRD measurements of the SL peak indicate a persisting CDW state above the thermal transition temperature²⁹.

Conclusion

In summary, we experimentally track the structural and electronic order parameters of a photoinduced CDW-to-metal transition in the rare-earth tritelluride TbTe₃, and reveal a close correspondence of the charge and lattice components of the CDW phase throughout the melting and initial recovery of order. By extracting the time-dependent electronic temperature, we demonstrated nonthermal CDW formation at electronic temperatures significantly above the thermodynamic transition temperature T_c . We attribute the dominating role of this behaviour to reduced lattice fluctuations compared to a scenario in which charges and lattice are in equilibrium above T_c . Since lattice fluctuations play a universal role in the CDW formation, the observed nonthermal stabilization mechanism should also apply to other material families. Moreover, we observed excitation-dependent collective dynamics of the charge order, closely connected to a coherent modulation of the periodic lattice distortion. We applied a tdGL framework to model the order-parameter dynamics and to describe the underlying transient potential energy surface, which governs the collective behaviour. Despite its simplicity of using a single degree of freedom, this phenomenological model reproduces all key observations. This suggests that mode-coupling³⁶ and inhomogeneities (defects) play only a secondary role in the dynamical melting and recovery of the CDW amplitude.

As any memory device relies on nonequilibrium properties, our results have strong implications for applications involving charge-ordering phenomena. A key parameter defining the persistence of the nonthermal stabilization is phonon-phonon coupling, as it dictates the lattice thermalization and thus the timescale on which the fluctuation background rises. Therefore, minimizing phonon-phonon coupling may be critical in the design of switchable CDW devices operating in nonequilibrium conditions⁶¹.

Methods

trARPES. Single crystals of TbTe₃ samples were grown by slow cooling of a binary melt³⁸. All experiments were carried out at $T = 100$ K. The ARPES measurements were performed in ultra-high vacuum $< 1 \times 10^{-10}$ mbar (samples cleaved in-situ), using a laser-based higher-harmonic-generation trARPES setup⁶² ($h\nu_{\text{probe}}=21.7$ eV, $h\nu_{\text{pump}}=1.55$ eV, 500 kHz repetition rate, $\Delta E \approx 175$ meV, $\Delta t \approx 35$ fs) and a SPECS Phoibos 150 hemispherical analyzer. The pump and probe spot sizes (FWHM) are $\approx 230 \times 200 \mu\text{m}^2$ and $\approx 70 \times 60 \mu\text{m}^2$. All discussed fluence values refer to the absorbed fluence F_{abs} . To estimate F_{abs} , the complex refractive index was determined via optical reflectivity measurements at $\lambda=800$ nm to $n=0.9$ and $k=2.6$.

trXRD. The trXRD measurements were carried out at the FEMTO hard X-ray slicing source

(X05LA) at the Swiss Light Source, Paul Scherrer Institut, Villigen, Switzerland⁶³. The utilized laser-sliced X-ray pulses ($h\nu_{\text{X-ray}}=7\text{ keV}$, $\Delta t \approx 120\text{ fs}$) feature the high stability of conventional synchrotron radiation and do not exhibit any relevant jitter in position, angle or wavelength. The diffracted X-ray intensity was recorded with an avalanche photodiode in an asymmetric diffraction geometry. A synchronized optical pump laser (10° angle of incidence, $h\nu_{\text{pump}}=1.55\text{ eV}$, $\Delta t \approx 110\text{ fs}$) was used to excite the system. The pump and probe spot sizes (FWHM) were $\approx 600 \times 600\text{ }\mu\text{m}^2$ and $\approx 250 \times 5\text{ }\mu\text{m}^2$. The X-ray extinction length was matched to the pump penetration depth of 25 nm by using a grazing angle of incidence of 0.5° .

Acknowledgements

We thank E.M. Bothschafter for support during the trXRD experiments. This work was funded by the Max Planck Society, the European Research Council (ERC) under the European Union’s Horizon 2020 research and innovation program (Grant No. ERC-2015-CoG-682843), the German Research Foundation (DFG) within the Emmy Noether program (Grant No. RE 3977/1), and the DFG research unit FOR 1700. Crystal growth and characterization at Stanford University (P.W. and I.R.F.) was supported by the Department of Energy, Office of Basic Energy Sciences under Contract No. DE-AC02-76SF00515. Part of this work was supported by the NCCR Molecular Ultrafast Science and Technology (Grant No. 51NF40-183615), a research instrument of the Swiss National Science Foundation (SNSF).

Data availability

The data that support the findings of this study are publicly available in Zenodo with the identifier doi:10.5281/zenodo.4106272⁶⁴.

Author contributions

Y.W.W, L.R., M.P., C.W.N. and J.M. carried out the trARPES experiments; L.R., V.E., M.P., J.R., D.L., M.K., M.S., E.A., S.L.J., P.B., G.I. and U.S. carried out the trXRD experiments; P.W. and I.R.F. provided the samples; J.M. analysed the data with support from L.R.; J.M. wrote the manuscript with support from L.R., R.E. and M.W.; all authors commented on the paper.

Competing Interests

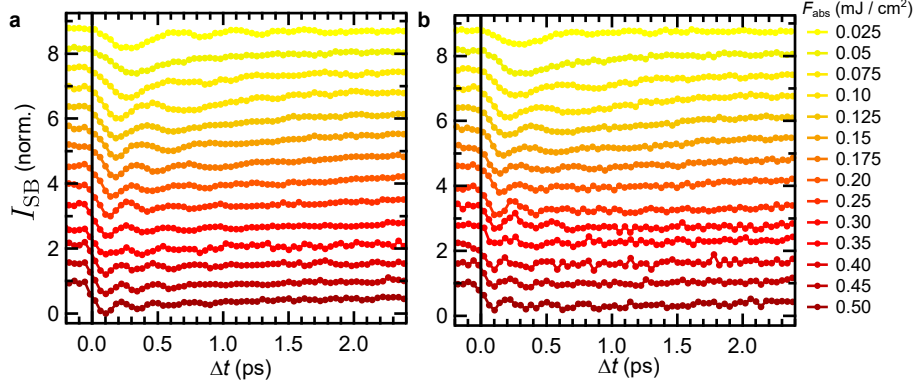
The authors declare no competing interests.

Correspondence

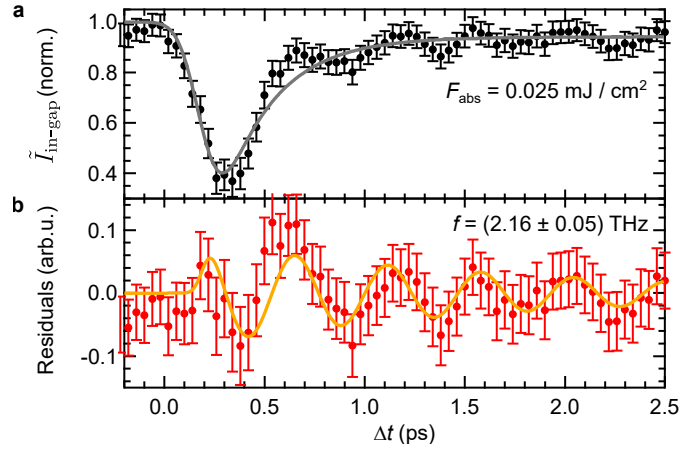
Correspondence should be addressed to maklar@fhi-berlin.mpg.de and rettig@fhi-berlin.mpg.de.

Supplementary Information for "Nonequilibrium Charge-Density-Wave Order Beyond the Thermal Limit"

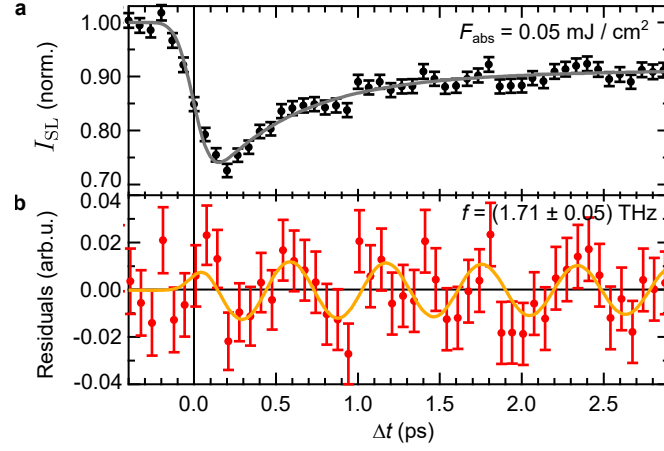
A Supplementary Figures



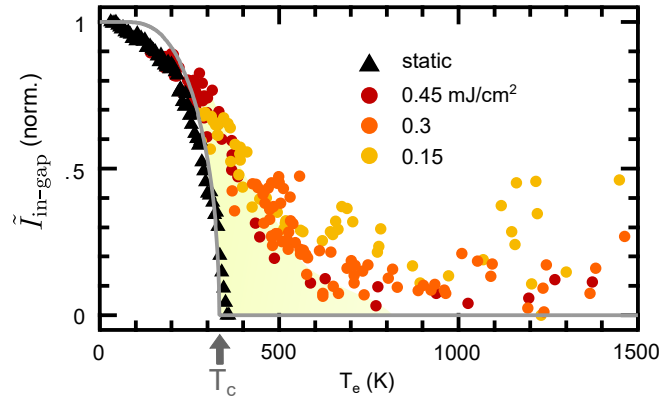
Supplementary Fig. 1: Shadow band intensity dynamics. Shadow band intensities extracted from (a) the nested (gapped) region of the FS, see box 2 in Fig. 2b, and (b) from the imperfectly nested (metallic) region, see box 3. Despite a slightly lower data quality in b, both shadow bands exhibit identical behaviour over the entire fluence range. The curves are vertically offset for clarity. For each curve, an intensity background extracted from a box slightly horizontally offset from the shadow band position is subtracted. Further, all curves are normalized by their respective intensities before excitation.



Supplementary Fig. 2: Electronic AM dynamics. (a) Time evolution of the inverted in-gap intensity after weak excitation. The grey line marks a double-exponential fit convolved with a Gaussian. (b) Fit residuals showing a pronounced amplitude mode in agreement with previous trARPES experiments^{6,65}, with a damped sinusoidal fit (orange curve). The error bars correspond to one standard deviation from electron counting statistics.



Supplementary Fig. 3: Structural AM dynamics. (a) Time evolution of the normalized $(2\ 10\ 1+q_{\text{CDW}})$ SL peak intensity after weak excitation. The grey line marks a double-exponential fit convolved with a Gaussian. The error bars correspond to one standard deviation from photon counting statistics. (b) The fit residuals indicate weak oscillations superimposed on the exponential decay, corresponding to a phonon mode that strongly couples to the CDW amplitude mode at 100 K, in agreement with previous optical and trXRD studies^{36,37,66,67}, with a damped sinusoidal fit (orange curve).



Supplementary Fig. 4: T -dependent CDW recovery dynamics. Inverted in-gap intensity of the dynamic CDW recovery versus extracted electronic temperatures for selected fluences. For reference, the static T -dependence is shown (black) with the BCS-like mean-field curve (grey). For clarity, the values of the dynamic traces for $t < 200$ fs (initial CDW melting) are omitted. The dynamic curves follow a universal recovery behaviour over a wide range of fluences. The region of nonthermal CDW order above the thermal critical temperature is shaded yellow. Normalization of the dynamic traces according to Fig. 3b.

B Details of the tdGL simulations of the electronic order parameter

To simulate the observed electron dynamics, we solve the following equation of motion based on the transient potential energy surface (Eq. 1)

$$\frac{\partial^2}{\partial t^2}\psi = \frac{\omega_{\text{AM}}^2}{2} \left((1 - \eta(t))\psi - \psi^3 \right) - \gamma \frac{\partial}{\partial t}\psi, \quad (3)$$

which yields the order parameter $\psi(t)$ used to simulate the diffracted intensities and the in-gap photoemission intensities. The initial conditions are chosen as

$$\psi = \sqrt{1 - \frac{T_{\text{base}}}{T_c}} \approx 0.84,$$

i.e., the static Ginzburg-Landau value corresponding to the temperature before excitation, and

$$\frac{\delta\psi}{\delta t} = 0.$$

We perform a global fit of the electronic in-gap dynamics $\tilde{I}_{\text{in-gap}}(t)$ over the full accessible fluence range (Fig. 2f) with the free parameters damping γ and scaling factor s of the nonthermal critical temperature, see Eq. 2, while the remaining input parameters are fixed (Supplementary Table 1). In order to fit the inverted in-gap intensity, the order-parameter simulations are normalized. To model the transient potential energy surface, see Eq. 1, we use the extracted electronic temperatures in a parametrized form, see Supplementary Note C. We find that the maximum electronic temperature yields a good description of the initial excited potential energy shape. This is evident from the saturation of $T_{\text{e,max}}$ in the high-fluence regime (see Supplementary Fig. 7c) that is accompanied by an upper limit of the initial coherent modulation frequency of the electronic order parameter. This also implies that the potential energy surface does not directly scale with the absorbed fluence $\eta \propto F$.

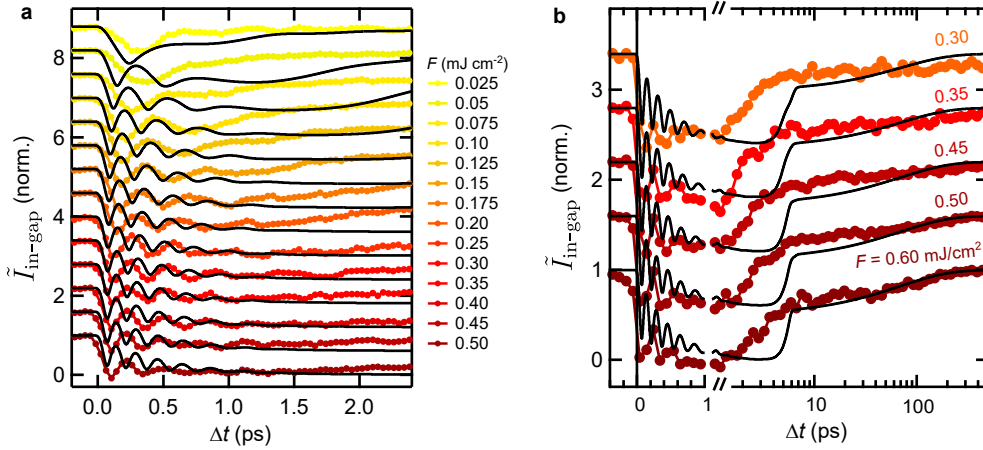
We aim to define the fit parameters as simple as possible; however, we can not reproduce the experimental data over the entire fluence- and temporal range with a single global damping constant. While γ correctly captures the initial damped modulations, a constant damping results in the reappearance of coherent oscillations in the high-fluence regime, when the potential transforms back from the high-symmetry to the double-well shape. To prevent this, we use an alternative global fit parameter γ_{rec} during the recovery (> 2 ps) in the high-fluence regime ($\geq 0.3 \text{ mJ cm}^{-2}$). In real systems, dephasing prevents the reappearance of coherent oscillations during the recovery.

We account for the inhomogeneous excitation profile, corresponding to the pump and probe spot sizes (FWHM) of $\approx 230 \times 200 \mu\text{m}^2$ and $\approx 70 \times 60 \mu\text{m}^2$, respectively, by averaging over multiple simulations with varying fluences (up to $\pm 7.5\%$ around the centre value). Finally, to account for the temporal resolution of the experiment, the simulations are convolved with a Gaussian (FWHM = 35 fs).

As illustrated in Fig. 3b, the transient CDW recovery strongly deviates from static (thermal) behaviour, which necessitates the introduction of a transiently increased critical temperature T_c^* in the tdGL simulations. To highlight the requirement of a transiently increased T_c^* , we perform additional simulations employing the constant equilibrium critical temperature T_c , while keeping the remaining parameters fixed as described above. As Supplementary Fig. 5 shows, this does not reproduce the experimental data, as (i) the simulated oscillation frequencies are strongly overestimated due to the increased slope of the underlying potential energy landscape (determined by $\eta(t)$) and (ii) the simulated recovery sets in only at $T_e < T_c$ – at a significant delay with respect to the experimental data.

Supplementary Table 1: Parameters of the tdGL simulations

Parameter	Value	Physical meaning
$\omega_{\text{AM}}/2\pi$	2.2 THz ³⁶	AM at 100 K
γ	4.4 THz	Damping
γ_{rec}	11.3 THz	Damping during the recovery > 2 ps in the overshoot regime
T_c	336 K ⁴⁰	Critical temperature of the CDW
s	1.22	Scaling factor of the rescaled critical temperature T_c^*
$\tau_{\text{ph-ph}}$	2.2 ps ²⁷	Decay constant of the rescaled critical temperature T_c^*



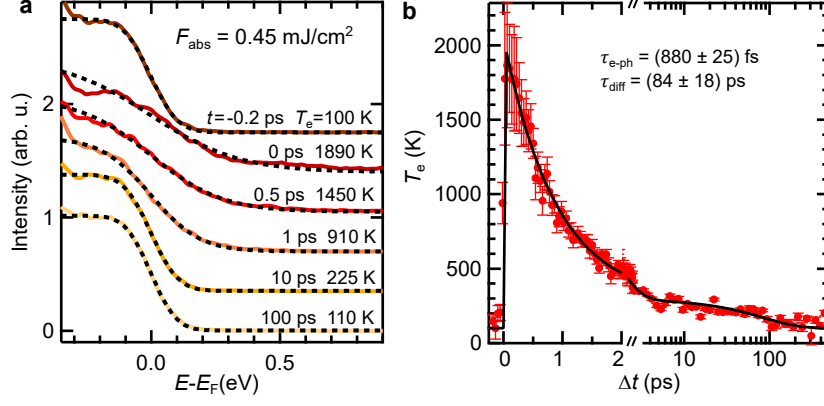
Supplementary Fig. 5: tdGL simulations using the constant equilibrium critical temperature T_c . (a) Experimental data analog to Fig. 2f and (b) to Fig. 3a of the main manuscript. The tdGL simulations are performed using the parameters as described above, however, using a fixed critical temperature of $T_c = 336$ K.

C Parametrization of the electronic temperatures

In the tdGL simulations, the electronic temperature $T_e(t)$ enters as an input parameter that determines the underlying potential shape. Thus, we extract the transient electronic temperatures from Fermi-Dirac fits of the quasiparticle energy distribution of the metallic region of the FS^{27,68}, as these values are more reliable than the approximation by the 3TM. For each dataset, the energy resolution ($\Delta E \approx 175$ meV) is determined from a fit to energy distribution curves (EDCs) before the arrival of the pump pulse, fixing the base temperature to $T_{\text{base}} = 100$ K. Then, the electronic temperature is extracted for varying delays, keeping the energy resolution fixed while using the position of the Fermi level and temperature as free fit parameters. Exemplary fits are shown in Supplementary Fig. 6a. A deviation from a thermal distribution appears for EDCs close to temporal pump-probe overlap, resulting in a large standard deviation of the extracted temperatures. Figure 6b depicts the electronic temperature evolution in the high-fluence regime. The relaxation of T_e features two distinct timescales, which we assign to the initial energy transfer from the electrons to specific optical phonons and a subsequent cooling of the thermalized system via diffusion.

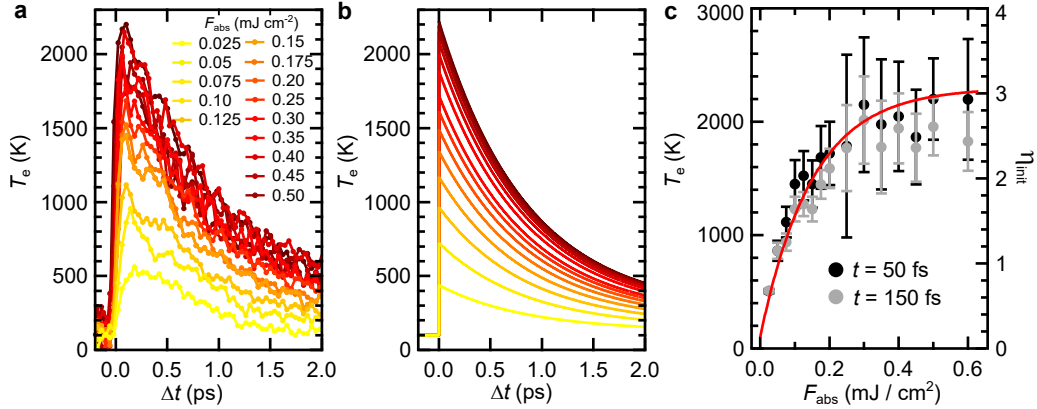
This fitting routine has been performed for all measured fluences in order to parametrize the fluence and time dependence of T_e , shown in Supplementary Fig. 7. The temporal evolution is approximated by a double-exponential decay:

$$T_e(t, F) = T_{\text{base}} + H(t) \cdot T_{\text{sat}}(F) \left[A_0 \cdot \exp(-t/\tau_{\text{e-ph}}) + (1 - A_0) \cdot \exp(-t/\tau_{\text{diff}}) \right] \quad (4)$$



Supplementary Fig. 6: Time-dependent Fermi-Dirac fits. (a) EDCs extracted from the metallic region of the FS with Fermi-Dirac fits for selected pump-probe delays. (b) Extracted electronic temperature as function of delay with biexponential decay fit (black curve). One standard deviation of the temperature fits are given as uncertainty.

with Heaviside step function $H(t)$, the excitation-dependent temperature increase T_{sat} discussed below, and the amplitude ratio between the fast (τ_{e-ph}) and slow (τ_{diff}) decay components. The values of the temperature parametrization are listed in Supplementary Table 2.



Supplementary Fig. 7: Electronic temperature parametrization. (a) Extracted temporal evolution of electronic temperatures and (b) parametrization by Supplementary Eq. 4. (c) Extracted electronic temperatures close to temporal pump-probe overlap versus fluence. The saturation model of the maximum electronic temperatures (Supplementary Eq. 6) is shown in red. One standard deviation of the temperature fits are given as uncertainty.

In the regime of strong excitation, the maximum electronic temperatures saturate at $T_{e,\text{max}}(t \approx 0 \text{ fs}) \approx 2300 \text{ K}$ (see Supplementary Fig. 7c). While the electronic system has not fully thermalized close to pump-probe overlap (and therefore electronic temperatures are ill-defined), we find that this saturation trend is also evident at later pump-probe delays. This saturation effect can be either due to a highly nonlinear electronic heat capacity or due to photobleaching. As the FS of TbTe₃ consists of metallic and CDW-gapped regions, the electronic heat capacity is expected to follow a linear metal-like temperature dependence with an additional nonlinear increase resulting from the redistribution of spectral weight due to the phase transition^{27,69}. Furthermore, our observations agree with the saturation plateau of excited quasiparticle intensity in the related compound LaTe₃⁵⁶. Such a fluence saturation trend of the electronic excitation level has also been observed in Blue Bronze²⁶.

We model the fluence-dependence of the temperature saturation as

$$T_{\text{sat}}(F) = T_0 \cdot [1 - \exp(-F/f)], \quad (5)$$

with the upper temperature limit T_0 and the fluence scaling factor f . The maximum electronic temperature is therefore given by

$$T_{\text{e,max}}(F) = T_{\text{base}} + T_{\text{sat}}. \quad (6)$$

Supplementary Table 2: Parametrization values of the electronic temperature.

Parameter	Value	Physical meaning
T_{base}	100 K	Base temperature of the sample
T_0	2200 K	Temperature limit of the saturation model
f	0.15 mJ cm^{-2}	Fluence scaling factor
$\tau_{\text{e-ph}}$	0.85 ps	Fast decay constant of the electronic temperature evolution
τ_{diff}	85 ps	Slow decay constant of the electronic temperature evolution
A_0	0.92	Amplitude ratio between the two components of the biexponential decay

D tdGL simulations of the structural order parameter

To simulate the trXRD measurements of the SL peak intensity, we have to account for the contribution of sub-surface layers of varying excitation densities due to the finite pump and probe beam penetration depths. We introduce a layered model, in which the tdGL equation of motion is solved for each individual layer. The diffracted X-ray beam corresponding to the $(2\ 10\ 1+q_{\text{CDW}})$ SL reflection leaves the sample at an exit angle of $\theta \approx 35^\circ$. As the lateral CDW correlation length L_{coh}^{40} is significantly larger than the effective penetration depth of the X-ray field $L_{\text{coh}} \gg 2\delta_{\text{X-ray}}/\sin\theta$, interference of different layers has to be considered^{23,70}. Thus, the total intensity is given by the coherent sum of all layers j of thickness d

$$I_{\text{SL}}(t) \propto \left(\sum_{j=0}^{\infty} \exp(-jd/2\delta_{\text{X-ray}}) \cdot \psi_j(t) \right)^2, \quad (7)$$

whereas the first term weights the contribution of each layer according to the X-ray penetration depth $\delta_{\text{X-ray}} = 25 \text{ nm}$. The initial excitation level of the first layer $\eta_{0,\text{init}}$ is calculated from the fluence-to-electronic-temperature calibration obtained from the trARPES data (see Supplementary Note C). The attenuation of the excitation of buried layers is given by Lambert-Beer's law $\eta_{j,\text{init}} = \eta_{0,\text{init}} \cdot \exp(-jd/\delta_{\text{pump}})$, with the penetration depth of the optical pulses $\delta_{\text{pump}} = 25 \text{ nm}$. We choose a layer thickness of $d = 1 \text{ nm}$ and sum the 250 topmost layers. To account for the temporal resolution of the experimental setup, the simulated intensity is convolved with a Gaussian (FWHM of 160 fs). In the regime of very weak excitation, the introduced model leads to artifacts, as the rescaling of T_c^* causes an initial increase of $\psi(t)$ in cases where the electronic temperature barely increases. To avoid these simulation artifacts from buried layers at very low excitation densities, the order parameter $\psi_j(t)$ of layers j with excitation levels $\eta_{j,\text{init}} < 0.25$ is fixed at the pre-excitation value $\psi_j(t < 0)$.

As we do not observe clear oscillations of I_{SL} upon strong excitation, we do not include the trXRD data in the global fitting procedure. Rather, we apply the parameters of the simulations of the electronic order parameter to the layered model. In agreement with previous studies, we find that the dominant oscillatory component of the SL peak intensity after weak excitation is a $\approx 1.7 \text{ THz}$ mode^{37,66}. As the AM softens upon cooling, it crosses the energy of this additional mode, leading to an anti-crossing behaviour. Due to their coupling, this phonon mode appears at the same wave vector as the CDW^{36,67}, see

Supplementary Fig. 3. Thus, we use $\omega_{\text{AM}} = 1.7$ THz to simulate $|\psi_s|$. Further, we omit the averaging over varying fluences, used in the simulations of the electronic order parameter. The remaining parameters are adopted from Supplementary Note B.

As discussed in the main text, surface steps may lead to unexcited sample areas. Therefore, a SL background persists even after strong excitation. To account for this, we rescale all structural intensity simulations by a global factor according to the maximum suppression of I_{SL} at the highest fluences.

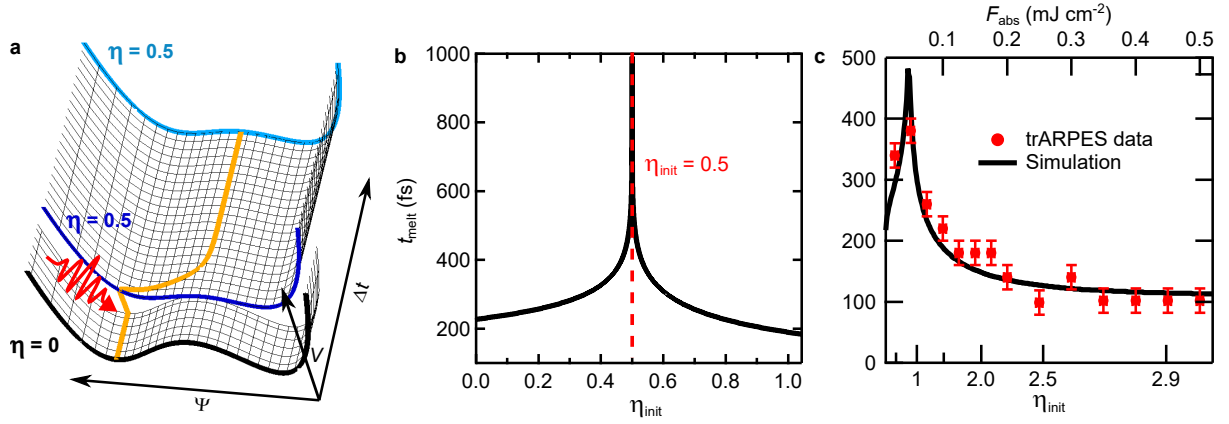
This layered model captures all main experimental features of I_{SL} , see Fig. 2h. The absence of the oscillatory component in the high-fluence regime is well reproduced by the simulations, and results from the limited temporal resolution and the superposition of layers with varying excitation densities. Further, the absence of a recovery after strong excitation for several ps is in agreement with the simulations, and results from a destructive interference of the contributions of different layers with opposite sign of ψ , corresponding to opposite sides of the underlying potential⁴⁸. In the low-fluence regime, the absolute intensities slightly deviate from the simulations. The absorbed fluence (determining the initial electronic temperature) is a highly sensitive input parameter of this model. Minor deviations between the fluence calibration of the trARPES and the trXRD setup have a major impact on the simulations. In addition, small uncertainties of the angle of incidence of the X-ray beam affect the penetration depth, a further sensitive parameter of this model.

E Critical slowing-down of the CDW melting and recovery

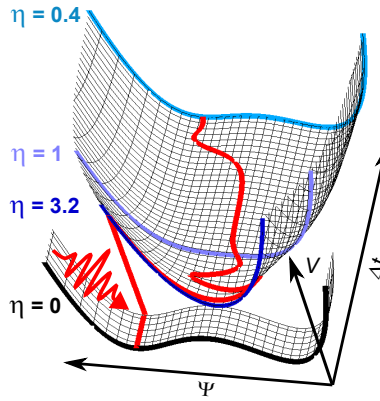
Critical slowing-down is a ubiquitous signature of phase transitions close to equilibrium⁷¹, and can also occur in a dynamical setting upon perturbation⁷². For several CDW systems, a dynamical slowing-down of the CDW melting after optical excitation in the regime of the threshold fluence has been observed^{56,73}. Here, we present a further instance of a dynamical slowing-down, which we discuss within the tdGL framework.

First, we utilize the tdGL formalism to study t_{melt} , i.e., the CDW melting time, as function of excitation density, shown in Supplementary Fig. 8b. For clarity, we turn off the relaxation of the potential energy surface after excitation ($\eta = \text{const}$), fix the critical temperature T_c^* , and suppress damping. In the regime of weak perturbation, the first minimum appears at half the period of the AM. With increasing fluence, the CDW melting time increases and finally diverges at $\eta = 0.5$. In the divergent case, see Supplementary Fig. 8a, the energy gain of the excitation is just enough so that the order parameter approaches the local maximum $|\psi| \approx 0$. Close to this metastable point, the potential energy surface is fairly flat, which leads to a dynamical slowing-down. However, when using realistic simulation parameters, such as a relaxing potential energy surface, and taking into account an inhomogeneous excitation profile, the divergence is strongly reduced, and the simulated melting time agrees with the experimental data (see Supplementary Fig. 8c).

A further dynamical slowing-down can occur during the recovery of the CDW. At specific fluences, when $|\psi| \approx 0$ and $\delta\psi/\delta t \approx 0$ at the same time as the potential regains the double-well shape ($\eta = 1$), the order parameter gets frozen, illustrated in Supplementary Fig. 9. Due to the weak curvature in the vicinity of $|\psi| = 0$, the system is trapped in a metallic phase, despite an emerging double-well potential. However, this divergence is difficult to observe experimentally, as it occurs at narrow fluence windows, and is, similar to the slowing-down of the CDW melting, suppressed by crystal defects, coupling to other phonon modes and an inhomogeneous excitation profile. This critical behaviour leads to a delayed onset of CDW recovery in the simulations as compared to the electronic CDW dynamics for certain fluences, see Fig. 2f (curve $F = 0.1$ mJ cm⁻²) and Fig. 3a.



Supplementary Fig. 8: Dynamic slowing-down of the CDW melting. (a) Transient potential and simulated order parameter (orange line) upon excitation corresponding to $\eta = 0.5$. (b) Time to reach the first local minimum as function of initial excitation η_{init} . Simulation parameters of a and b: $\gamma = 0$ THz, $T_c^* = \text{const} = 336$ K and $\tau_{\text{e-ph}} = \tau_{\text{diff}} = \infty$. (c) Initial minima of the inverted in-gap intensity, see Fig. 2f, versus absorbed fluence and initial excitation η_{init} . Results of the tdGL simulations with realistic model parameters (see Supplementary Note B) are shown in black. The error bars of the experimentally extracted melting times represent the temporal width (FWHM) of the XUV probe pulses.



Supplementary Fig. 9: Dynamic slowing-down of the CDW recovery. Transient potential and simulated order-parameter pathway of the dynamical slowing-down during the CDW recovery. For specific excitation conditions, the order-parameter dynamics critically slow down during recovery of the CDW double-well potential. Despite the appearance of the double-well shape for $\eta < 1$ (purple line), the order parameter can get trapped at the metastable point $|\psi| \approx 0$, before it relaxes into one of the global minima. Model parameters are chosen analogous to Supplementary Note B. To demonstrate a pronounced slowing-down, the averaging over multiple curves with varying fluences is omitted.

References

1. Motizuki, K. *Structural phase transitions in layered transition metal compounds* (Springer Science & Business Media, 1986).
2. Gruner, G. *Density waves in solids* (CRC press, 1994).
3. Pouget, J.-P. The Peierls instability and charge density wave in one-dimensional electronic conductors. *Comptes Rendus Physique* **17**, 332–356 (2016).
4. Demsar, J., Biljakovic, K. & Mihailovic, D. Single particle and collective excitations in the one-dimensional charge density wave solid $\text{K}_{0.3}\text{MoO}_3$ probed in real time by femtosecond spectroscopy. *Physical review letters* **83**, 800 (1999).
5. Perfetti, L. *et al.* Time Evolution of the Electronic Structure of 1T-TaS₂ through the Insulator-Metal Transition. *Physical review letters* **97**, 067402 (2006).
6. Schmitt, F. *et al.* Transient electronic structure and melting of a charge density wave in TbTe₃. *Science* **321**, 1649–1652 (2008).
7. Eichberger, M. *et al.* Snapshots of cooperative atomic motions in the optical suppression of charge density waves. *Nature* **468**, 799–802 (2010).
8. Möhr-Vorobeva, E. *et al.* Nonthermal melting of a charge density wave in TiSe₂. *Physical review letters* **107**, 036403 (2011).
9. Hellmann, S. *et al.* Time-domain classification of charge-density-wave insulators. *Nature communications* **3**, 1–8 (2012).
10. Sohrt, C., Stange, A., Bauer, M. & Rossnagel, K. How fast can a Peierls–Mott insulator be melted? *Faraday discussions* **171**, 243–257 (2014).
11. Huber, T. *et al.* Coherent structural dynamics of a prototypical charge-density-wave-to-metal transition. *Physical review letters* **113**, 026401 (2014).
12. Porer, M. *et al.* Non-thermal separation of electronic and structural orders in a persisting charge density wave. *Nature materials* **13**, 857–861 (2014).
13. Rettig, L. *et al.* Persistent order due to transiently enhanced nesting in an electronically excited charge density wave. *Nature communications* **7**, 1–6 (2016).
14. Monney, C. *et al.* Revealing the role of electrons and phonons in the ultrafast recovery of charge density wave correlations in 1T- TiSe₂. *Physical Review B* **94**, 165165 (2016).
15. Yang, L. *et al.* Bypassing the structural bottleneck in the ultrafast melting of electronic order. *Physical Review Letters* **125**, 266402 (2020).
16. Tsuji, N., Eckstein, M. & Werner, P. Nonthermal antiferromagnetic order and nonequilibrium criticality in the Hubbard model. *Physical review letters* **110**, 136404 (2013).
17. Stojchevska, L. *et al.* Ultrafast switching to a stable hidden quantum state in an electronic crystal. *Science* **344**, 177–180 (2014).
18. Zhang, J. *et al.* Cooperative photoinduced metastable phase control in strained manganite films. *Nature materials* **15**, 956–960 (2016).
19. Gerasimenko, Y. A., Karpov, P., Vaskivskiy, I., Brazovskii, S. & Mihailovic, D. Intertwined chiral charge orders and topological stabilization of the light-induced state of a prototypical transition metal dichalcogenide. *npj Quantum Materials* **4**, 1–9 (2019).
20. Fausti, D. *et al.* Light-induced superconductivity in a stripe-ordered cuprate. *science* **331**, 189–191 (2011).

21. Wandel, S. *et al.* Light-enhanced Charge Density Wave Coherence in a High-Temperature Superconductor. *arXiv preprint arXiv:2003.04224* (2020).
22. Kogar, A. *et al.* Light-induced charge density wave in LaTe_3 . *Nature Physics* **16**, 159–163 (2020).
23. Beaud, P. *et al.* A time-dependent order parameter for ultrafast photoinduced phase transitions. *Nature materials* **13**, 923–927 (2014).
24. Wall, S. *et al.* Ultrafast disordering of vanadium dimers in photoexcited VO_2 . *Science* **362**, 572–576 (2018).
25. Nicholson, C. W. *et al.* Beyond the molecular movie: Dynamics of bands and bonds during a photoinduced phase transition. *Science* **362**, 821–825 (2018).
26. Neugebauer, M. J. *et al.* Optical control of vibrational coherence triggered by an ultrafast phase transition. *Physical Review B* **99**, 220302 (2019).
27. Dolgirev, P. E. *et al.* Amplitude dynamics of the charge density wave in LaTe_3 : Theoretical description of pump-probe experiments. *Physical Review B* **101**, 054203 (2020).
28. Mitrano, M. *et al.* Possible light-induced superconductivity in K_3C_{60} at high temperature. *Nature* **530**, 461–464 (2016).
29. Singer, A. *et al.* Photoinduced enhancement of the charge density wave amplitude. *Physical review letters* **117**, 056401 (2016).
30. Nicholson, C. *et al.* Ultrafast spin density wave transition in chromium governed by thermalized electron gas. *Physical review letters* **117**, 136801 (2016).
31. Cavalleri, A. Photo-induced superconductivity. *Contemporary Physics* **59**, 31–46 (2018).
32. Tengdin, P. *et al.* Critical behavior within 20 fs drives the out-of-equilibrium laser-induced magnetic phase transition in nickel. *Science advances* **4**, 9744 (2018).
33. Endres, M. *et al.* The ‘Higgs’ amplitude mode at the two-dimensional superfluid/Mott insulator transition. *Nature* **487**, 454–458 (2012).
34. Matsunaga, R. *et al.* Higgs amplitude mode in the BCS superconductors $\text{Nb}_{1-x}\text{Ti}_x\text{N}$ induced by terahertz pulse excitation. *Physical review letters* **111**, 057002 (2013).
35. Torchinsky, D. H., Mahmood, F., Bollinger, A. T., Božović, I. & Gedik, N. Fluctuating charge-density waves in a cuprate superconductor. *Nature materials* **12**, 387–391 (2013).
36. Yusupov, R., Mertelj, T., Chu, J.-H., Fisher, I. & Mihailovic, D. Single-Particle and Collective Mode Couplings Associated with 1-and 2-Directional Electronic Ordering in Metallic RTe_3 ($\text{R} = \text{Ho, Dy, Tb}$). *Physical review letters* **101**, 246402 (2008).
37. Trigo, M. *et al.* Coherent order parameter dynamics in SmTe_3 . *Physical Review B* **99**, 104111 (2019).
38. Ru, N. & Fisher, I. Thermodynamic and transport properties of YTe_3 , LaTe_3 , and CeTe_3 . *Physical Review B* **73**, 033101 (2006).
39. Brouet, V. *et al.* Angle-resolved photoemission study of the evolution of band structure and charge density wave properties in RTe_3 ($\text{R} = \text{Y, La, Ce, Sm, Gd, Tb, and Dy}$). *Physical Review B* **77**, 235104 (2008).
40. Ru, N. *et al.* Effect of chemical pressure on the charge density wave transition in rare-earth tritellurides RTe_3 . *Physical Review B* **77**, 035114 (2008).
41. Maschek, M. *et al.* Wave-vector-dependent electron-phonon coupling and the charge-density-wave transition in TbTe_3 . *Physical Review B* **91**, 235146 (2015).

42. Laverock, J. *et al.* Fermi surface nesting and charge-density wave formation in rare-earth tritellurides. *Physical Review B* **71**, 085114 (2005).
43. Overhauser, A. Observability of charge-density waves by neutron diffraction. *Physical Review B* **3**, 3173 (1971).
44. Voit, J. *et al.* Electronic structure of solids with competing periodic potentials. *Science* **290**, 501–503 (2000).
45. Rettig, L., Chu, J.-H., Fisher, I., Bovensiepen, U. & Wolf, M. Coherent dynamics of the charge density wave gap in tritellurides. *Faraday discussions* **171**, 299–310 (2014).
46. Vogelgesang, S. *et al.* Phase ordering of charge density waves traced by ultrafast low-energy electron diffraction. *Nature Physics* **14**, 184–190 (2018).
47. Zong, A. *et al.* Evidence for topological defects in a photoinduced phase transition. *Nature Physics* **15**, 27–31 (2019).
48. Trigo, M. *et al.* Ultrafast formation of domain walls of a charge density wave in SmTe₃. *Physical Review B* **103**, 054109 (2021).
49. Yusupov, R. *et al.* Coherent dynamics of macroscopic electronic order through a symmetry breaking transition. *Nature Physics* **6**, 681–684 (2010).
50. Schaefer, H., Kabanov, V. V. & Demsar, J. Collective modes in quasi-one-dimensional charge-density wave systems probed by femtosecond time-resolved optical studies. *Physical Review B* **89**, 045106 (2014).
51. Perfetti, L. *et al.* Ultrafast electron relaxation in superconducting Bi₂Sr₂CaCu₂O_{8+δ} by time-resolved photoelectron spectroscopy. *Physical review letters* **99**, 197001 (2007).
52. Johnson, S. L. *et al.* Watching ultrafast responses of structure and magnetism in condensed matter with momentum-resolved probes. *Structural Dynamics* **4**, 061506 (2017).
53. Tao, Z., Han, T.-R. T. & Ruan, C.-Y. Anisotropic electron-phonon coupling investigated by ultrafast electron crystallography: Three-temperature model. *Physical Review B* **87**, 235124 (2013).
54. Nicholson, C. W. *et al.* Excited-state band mapping and momentum-resolved ultrafast population dynamics in In/Si (111) nanowires investigated with XUV-based time-and angle-resolved photoemission spectroscopy. *Physical Review B* **99**, 155107 (2019).
55. Storeck, G. *et al.* Structural dynamics of incommensurate charge-density waves tracked by ultrafast low-energy electron diffraction. *Structural Dynamics* **7**, 034304 (2020).
56. Zong, A. *et al.* Dynamical slowing-down in an ultrafast photoinduced phase transition. *Physical review letters* **123**, 097601 (2019).
57. Arguello, C. *et al.* Visualizing the charge density wave transition in 2H-NbSe₂ in real space. *Physical Review B* **89**, 235115 (2014).
58. Fang, A., Straquadine, J. A., Fisher, I. R., Kivelson, S. A. & Kapitulnik, A. Disorder-induced suppression of charge density wave order: STM study of Pd-intercalated ErTe₃. *Physical Review B* **100**, 235446 (2019).
59. Waldecker, L., Bertoni, R., Ernstorfer, R. & Vorberger, J. Electron-phonon coupling and energy flow in a simple metal beyond the two-temperature approximation. *Physical Review X* **6**, 021003 (2016).
60. Yamaji, K. First-order phase transition boundary between superconducting and SDW phases in the bechgaard salts. *Journal of the Physical Society of Japan* **52**, 1361–1372 (1983).

61. Vaskivskiy, I. *et al.* Controlling the metal-to-insulator relaxation of the metastable hidden quantum state in 1T-TaS₂. *Science advances* **1**, e1500168 (2015).
62. Puppín, M. *et al.* Time-and angle-resolved photoemission spectroscopy of solids in the extreme ultraviolet at 500 kHz repetition rate. *Review of Scientific Instruments* **90**, 023104 (2019).
63. Ingold, G. *et al.* Technical Report: FEMTO: A Sub-ps Tunable Hard X-ray Undulator Source for Laser/X-ray Pump-Probe Experiments at the SLS. *Synchrotron Radiation News* **20**, 35–39 (2007).
64. Maklar, J. *et al.* Time- and angle-resolved photoemission spectroscopy data and time-resolved X-ray diffraction data of TbTe₃ version 1.0.0 (Zenodo, Oct. 2020). <https://doi.org/10.5281/zenodo.4106272>.
65. Schmitt, F. *et al.* Ultrafast electron dynamics in the charge density wave material TbTe₃. *New Journal of Physics* **13**, 063022 (2011).
66. Moore, R. *et al.* Ultrafast resonant soft x-ray diffraction dynamics of the charge density wave in TbTe₃. *Physical Review B* **93**, 024304 (2016).
67. Maschek, M. *et al.* Competing soft phonon modes at the charge-density-wave transitions in DyTe₃. *Physical Review B* **98**, 094304 (2018).
68. Wang, Y. *et al.* Measurement of intrinsic Dirac fermion cooling on the surface of the topological insulator Bi₂Se₃ using time-resolved and angle-resolved photoemission spectroscopy. *Physical Review Letters* **109**, 127401 (2012).
69. Lin, Z., Zhigilei, L. V. & Celli, V. Electron-phonon coupling and electron heat capacity of metals under conditions of strong electron-phonon nonequilibrium. *Physical Review B* **77**, 075133 (2008).
70. Rettig, L. *et al.* Itinerant and localized magnetization dynamics in antiferromagnetic Ho. *Physical review letters* **116**, 257202 (2016).
71. Goldenfeld, N. *Lectures on phase transitions and the renormalization group* (CRC Press, 1992).
72. Dolgirev, P. E., Michael, M. H., Zong, A., Gedik, N. & Demler, E. Self-similar dynamics of order parameter fluctuations in pump-probe experiments. *Physical Review B* **101**, 174306 (2020).
73. Tomeljak, A. *et al.* Dynamics of photoinduced charge-density-wave to metal phase transition in K_{0.3}MoO₃. *Physical review letters* **102**, 066404 (2009).